Energy & Environmental Science

ROYAL SOCIETY OF CHEMISTRY

PAPER

View Article Online
View Journal

Cite this: DOI: 10.1039/d0ee03801f

Photoacoustic and piezo-ultrasound hybrid-induced energy transfer for 3D twining wireless multifunctional implants†

Laiming Jiang, ‡*[abc] Gengxi Lu,‡[ab] Yang Yang,[d] Yushun Zeng,[a] Yizhe Sun,[a] Runze Li,[ab] Mark S. Humayun,[abe] Yong Chen*[c] and Qifa Zhou*[ab]

Received 3rd December 2020,
Accepted 21st January 2021

DOI: 10.1039/d0ee03801f

rsc.li/ees

Ultrasound-induced energy transfer (UET) represents an emerging technology that can be integrated into implantable medical systems for wireless power and information communication applications. However, the spatial–temporal resolution, directivity, and versatility of traditional piezo-ultrasound systems are generally limited. Here, we describe the novel design and implementation of a hybrid-induced energy transfer strategy using photoacoustic (PA) and piezo-ultrasound (PU) technology in a 3D twining wireless implant, which shows multi-mode transmission advantages, with high power, better resolution, and flexible directivity. This new ultrasonic system exploits a focused ring piezo-transducer and a miniaturized fiber-photoacoustic converter as the hybrid acoustic source and a (K,Na)NbO_3-based lead-free linear piezo-array as the harvester. Complying with FDA regulations, hybrid-induced multifunctionality, such as stable powering (~21.3 mW cm^{-2}) and the high-resolution signal communication (signal-to-noise ratio: ~22.5 dB) of a two-dimensional image, was demonstrated *ex vivo* using 12 mm-thick porcine tissue. The 3D twining design also ensures that the device can achieve stable energy harvesting without operational difficulties, a unique advantage that can facilitate its future clinical application.

Broader context

UET has become an attractive topic for biomedical-related functional applications. Here, a hybrid-induced energy transfer strategy using photoacoustic (PA) and piezo-ultrasound (PU) technology in 3D twining wireless implants was proposed and implemented to solve issues relating to the portability, resolution, and multifunctionality (such as stable energy transfer, high-resolution communication, *etc.*) of traditional ultrasound systems. This novel ultrasonic system exploits a focused ring piezo-transducer and a miniaturized fiber-photoacoustic converter as the outer acoustic source and a 1 × 13 (K,Na)NbO_3-based lead-free twining piezo-array as the harvester. To the best of our knowledge, this is the very first time that PA and PU hybrid-induced UET has been combined with transcutaneous energy transfer for use in multifunctional implants, with the realization of stable wireless powering and high-resolution signal communication *ex vivo*. Additionally, a flexible design, with a bio-inspired 3D twining array and the strategic material integration of new (K,Na)NbO_3-based lead-free micro-composites, was adopted to ensure stable and safe energy harvesting, innovatively expanding the applications of biocompatible piezo-materials and devices.

[a] *Department of Biomedical Engineering, Viterbi School of Engineering, University of Southern California, Los Angeles, California 90089, USA. E-mail: qifazhou@usc.edu*

[b] *Roski Eye Institute, Department of Ophthalmology, Keck School of Medicine, University of Southern California, Los Angeles, California 90033, USA. E-mail: lj_456@usc.edu*

[c] *Epstein Department of Industrial and Systems Engineering, Viterbi School of Engineering, University of Southern California, Los Angeles, California 90089, USA. E-mail: yongchen@usc.edu*

[d] *Department of Mechanical Engineering, San Diego State University, San Diego, California 92182, USA*

[e] *Allen and Charlotte Ginsburg Institute for Biomedical Therapeutics, University of Southern California, Los Angeles, California 90089, USA*

† Electronic supplementary information (ESI) available. See DOI: 10.1039/d0ee03801f

‡ Laiming Jiang and Gengxi Lu contributed equally.

Introduction

Implantable biomedical devices (IBDs), such as cardioverter defibrillators,[1] cardiac pacemakers,[2] and neurostimulators,[3] have brought numerous medical advances in improving quality of life and extending human lifespans. Up to now, most IBDs are still powered by batteries that may need surgical interventions for their periodic replacement, resulting in non-negligible risks and costs.[4] New powering strategies based on inductive coupling technology[5] and self-powered systems[6,7] have been developed to remove batteries and to expand the functions of implants.[8] The former approach is highly sensitive to the alignment and distance between the coils and will produce

excessive heat in tissue, thereby affecting the immune system and metabolism.[9] The latter method mainly converts biological kinetic energy into electrical energy through piezoelectric and triboelectric systems. Nevertheless, these systems commonly suffer from limitations relating to the general implantation location, specific implant site, and uncertain output power from these devices. Additionally, a great deal of internal resistance (tens of megaohms) is generally obtained in traditional piezoelectric and triboelectric devices due to low-frequency body movements, resulting in limited power output.[10] From this perspective, both technologies raise safety and efficiency concerns.

Ultrasound-induced energy transfer (UET), which uses ultrasonic waves to carry input energy and propagate it to an implant site, has become an attractive strategy in the field of wireless powering, healthcare monitoring, and information communication.[9,11–14] Ultrasound is safe and non-invasive in most medical applications and it has long been used in biological diagnosis and therapeutics.[15] The attenuation of ultrasonic energy in biological tissue is much lower than that of electromagnetic radiation, which not only reduces unnecessary energy dissipation but also enables a deeper travel depth at a given power. Additionally, external ultrasonic sources can deliver adjustable and long-term sustainable power transmission *in vivo*, independently of the implant site, organ shape, and environmental transparency. UET based on piezoelectric and capacitive triboelectric technologies for powering implants has been demonstrated before.[9,13,16] However, these UET systems used heavy and bulky piezo-ultrasound (PU) transducers to transfer energy, and the transducers must be held stable and maintain a favorable angle to achieve optimal performance. The cumbersome nature of the alignment process is greatly increased due to the visual invisibility of the ultrasonic field. Additionally, the spatial–temporal resolution of the ultrasound waves generated by traditional PU transducers is generally limited, which is an undesirable feature for spatially–temporally confined neural stimulation and signal communication.[17] In‘ order to achieve portable, precise, and multi-mode energy transfer, new energy transfer strategies and well-designed device structures should be explored to expand the functionality of UET.

An alternative method of generating ultrasound waves is through the photoacoustic (PA) (also referred to as optoacoustic or thermoacoustic) effect.[18,19] The PA wave excitation process generally starts with pulsed light irradiating the absorber, yielding transient heating and thermal expansion and producing high-resolution ultrasound with a short pulse length on the time scale (Note S1, ESI†).[20,21] Different from a PU transducer, PA excitation can be based on a miniaturized and portable fiber-photoacoustic converter, so that the signal can be precisely orientated toward the target due to the high spatial accuracy of the light beam. Additionally, the PA effect possesses super weak directivity, that is, its performance is unrelated to the laser incident angle. In recent years, the PA effect has attracted increasing attention in the fields of medical imaging and translational medicine,[22,23] such as imaging brain structures in a non-invasive manner.[24] Despite the merits of the PA effect in medicine, this technique has not been used for constructing an energy transfer system for wireless implants. The latest progress in the development of PA materials has achieved highly efficient PA conversion.[25,26] The pulsed light excitation of these PA materials produces high-amplitude ultrasonic waves, which enables effective energy transfer.

Here, we report a hybrid-induced energy strategy using PA and PU technology in flexible and bio-inspired 3D twining multifunctional implants, overcoming the limitations of traditional ultrasound systems and thereby forming a new wireless platform with the combined advantages of high power, better spatial–temporal resolution, portability, and versatility. The newly designed architecture is configured with a focused ring piezo-transducer and a miniaturized fiber-photoacoustic converter as the hybrid acoustic source to provide multimodal transmittable ultrasound power. To the best of our knowledge, this is the very first time that the PA effect has been combined with transcutaneous energy transfer for use in implants. The ultrasound harvester exploits a 1×13 linear array of thin and performance-optimized lead-free 1–3 piezo-composites as the active elements; these were interconnected *via* a flexible wavy interconnection and encapsulated in a low-modulus elastomer. The integrated lead-free energy harvesting (LFEH) device is capable of sensing transmitted PA and PU waves from tens of millimeters away and converting them into tunable electricity. The transfer combines PA and PU induced characteristics, and it is suitable for portable multi-functional applications, such as the continuous charging of implant batteries and high-resolution information communication. Due to the thin profile with mechanical properties similar to those of organ tissue, the flexible array can ensure 3D twining on the organ surface, achieving ultrasound capture from multiple angles without operational difficulties. Systematic studies, including structural optimization, the powering of electronics, transcutaneous transmission, signal communication *ex vivo*, and safety analysis, were conducted to evaluate its potential applications. This hybrid-induced energy transfer strategy opens up opportunities for a future generation of wireless biomedical implants that are portable, stable, and multifunctional.

Results and discussion

The device design and structural optimization of the 3D twining LFEH device

The PA and PU hybrid-induced LFEH device involves the hybridization of high-performance rigid $(K,Na)NbO_3$ (KNN)-based lead-free piezo-elements with soft structural components. A schematic diagram of the 3D twining device is demonstrated in Fig. 1a. All the piezo-elements are connected in parallel *via* an island-bridge structural matrix and arranged into a 1×13 linear array with a pitch of 3.5 mm (1.5×1.5 mm^2 element footprint with a spacing of 2 mm) based on a trade-off between the twining flexibility and effective piezo-element density of the device (a schematic diagram of the fabrication

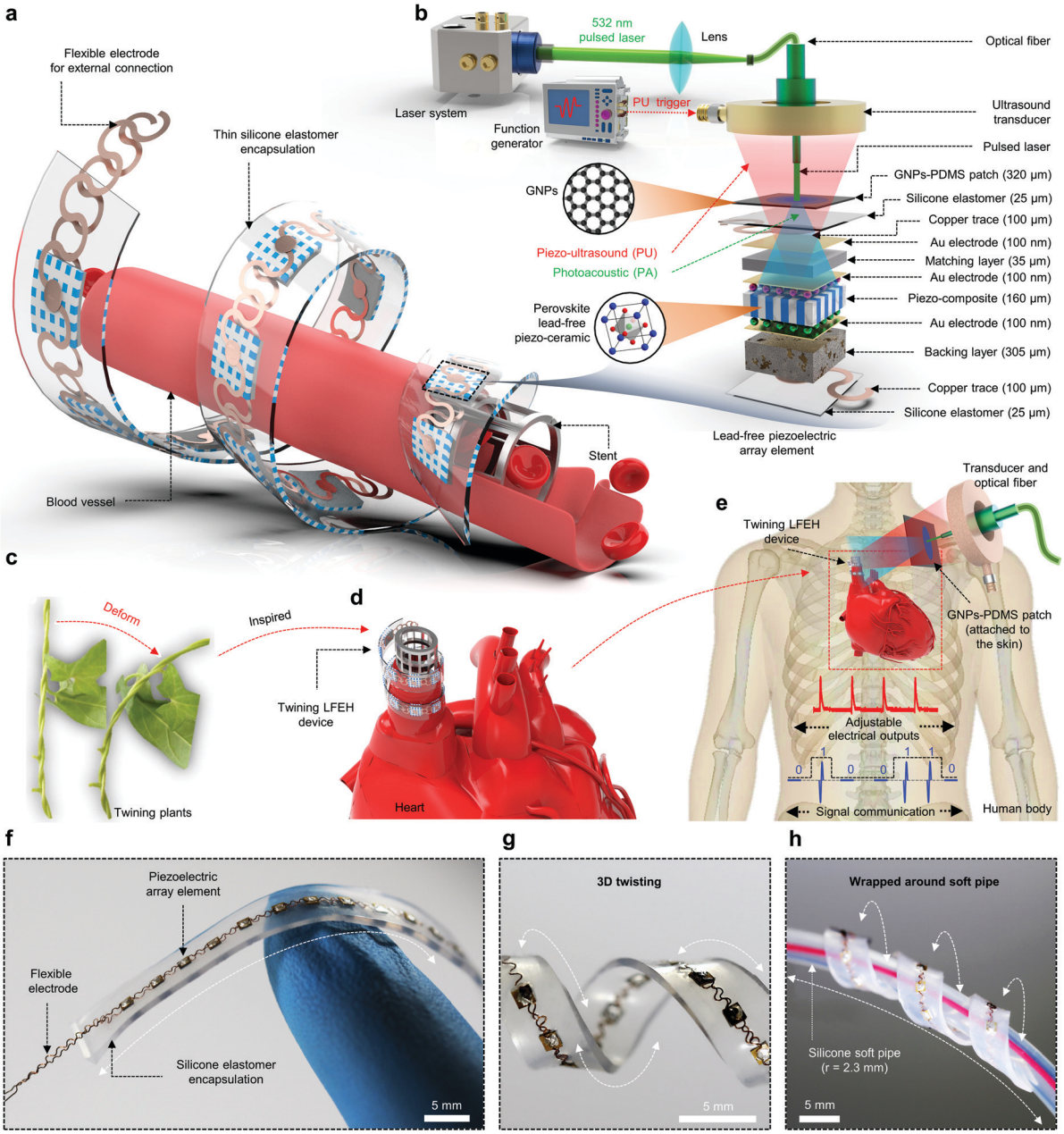

Fig. 1 Schematic diagrams and the design of the PU and PA hybrid-induced 3D twining LFEH device. (a) A schematic diagram of the design of the twining LFEH device with the key components labeled. (b) Exploded schematic diagrams of the PU and PA hybrid-induced process and each component in a piezo-element. (c) Optical images of twining plants during deformation. Reproduced with permission.[28] Copyright 2019, AAAS. (d and e) Schematic diagrams showing the twining-plant-inspired device wrapped around a blood vessel. (f–h) Optical images of the LFEH device when (f) placed on a finger, (g) undergoing 3D twisting, and (h) wrapped around a silicone soft pipe, demonstrating the mechanical compliance and robustness of the device.

process is given in Fig. S1, ESI†). Each island hosts a rigid piezo-element with a 1.5 × 1.5 mm^2 footprint to allow a sufficient sensing area (Fig. 1b). Wavy bridges that are inspired by the flexible ultrasound array reported by Xu *et al.*[27] can unfold to accommodate externally applied strain, with limited strain in the components themselves. Consequently, the array is rigid locally but flexible globally, and can be twisted and wrapped around the target object. This 3D twining design is inspired by the twining plants that are commonly found in nature, which use soft rhizomes to adaptively form a spiral configuration to maintain stability (Fig. 1c).[28] In this way, flexible twiners can capture more sunshine without losing stability, even under large deformation. Analogously, the bio-inspired twining harvester can also harvest acoustic energy transmitted from multiple directions to enhance the operational flexibility and stability when implanted in the human body (Fig. 1d and e), without the need for tedious manual positioning.

A copper wire with a diameter of 100 μm was selected to manufacture the wavy electrodes for interconnecting the piezo-elements and the external circuit (for detailed discussion of the

manufacturing process, see Experimental section). Both the top and bottom electrodes are routed to the same plane *via* a parallel interconnect for ease of electrical bonding and improved mechanical strength. The acoustic-induced accumulated electron flow between the two electrodes occurred *via* an external circuit. Then, the whole array was encapsulated in a silicone elastomer (Ecoflex 00-30) with a modulus ($\sim$0.125 MPa)[29] lower than that of biological tissue (*e.g.*, human skin: $\sim$0.5–1.95 MPa).[30] The top and bottom elastomer membranes are only 25 μm thick due to a trade-off between mechanical strength and adequate ultrasound penetration. The hydrophobic properties of the elastomer membrane provide a barrier to moisture, which protects the components from possible fluid corrosion (Fig. S2, ESI†). Upon combining geometrical and acoustic designs, the total thickness of the windable device is $\sim$750 μm (the thickness and material composition of each component in the device are shown in Fig. S3, ESI†). Due to its mechanical flexibility, the as-fabricated energy harvesting array can be bent (Fig. 1f), endure twisting (Fig. 1g), and be wrapped seamlessly on the surfaces of soft targets (Fig. 1h), showing its potential advantage of being able to harvest ultrasound from multiple angles.

As the core components of the energy receiver, the piezo-elements in a layer convert acoustic-induced mechanical vibration into electrical potential. The efficiency of this process can be optimized *via* designing piezoelectric composite microstructures. Piezoelectric energy harvesters for ultrasound-induced wireless-powering implants have already been demonstrated.[14,16,31] However, these harvesters mainly used lead zirconate titanate (PZT), which is questionable for ecological/biological applications due to the biological hazards associated with lead-based materials and the express provisions of Restriction of Hazardous Substances (RoHS) directive, which restricts the use of specific hazardous materials in electrical and electronic products. Therefore, KNN-based lead-free piezoceramics that possess environmental friendliness, biocompatibility, and good electrical properties have been demonstrated and developed into the most promising alternatives to lead-based examples,[32,33] especially for implantable medical devices that require direct contact with the human body.[34,35] KNN-based lead-free piezoceramics are currently quite comparable to PZT in terms of the d_{33} piezoelectric coefficient, and higher d_{33} values have been obtained from textured KNN-based ceramics.[36] In this work, a new KNN-based lead-free piezoceramic (Fe_2O_3-added (K,Na)(Nb,Sb)O_3–(Bi,Na)ZrO_3, abbreviated as F-KNN) with a high piezoelectric coefficient (d_{33}: $\sim$471 pC N^{-1}) was first synthesized, and three kinds of piezo-elements with different microstructures (a pure ceramic layer, a 2–2 composite layer, and a 1–3 composite layer) were further manufactured through a modified dicing-and-filling technique (Fig. 2a) to optimize the device performance. As presented in the X-ray diffraction (XRD) pattern and a scanning electron microscopy (SEM) image (Fig. S4, ESI†), our synthesized F-KNN sample exhibits a typical perovskite structure with multiphase coexistence and a dense ceramic body, thus ensuring excellent piezo-element performance.

1–3 piezo-composites consist of piezo-micropillars in a periodic configuration embedded in a passive epoxy matrix, maintaining the good piezoelectric properties of the ceramic pillars and exhibiting the low acoustic impedance required for good matching with human tissue, in addition to enhanced electromechanical coupling in the thickness mode.[37,38] Most importantly, the elastic and piezoelectric properties of 1–3 composites can also be tailored *via* changing the volume fraction and periodicity to optimize device performance.[39] According to the series and parallel models demonstrated by Chan and Unsworth,[40] the electrical and acoustic properties of composites can be calculated theoretically. The permittivity ε, electromechanical coupling factor k, acoustic impedance Z_a, and voltage factor g of the composites are functions of the piezoceramic volume fraction (v) (Note S2, ESI†). Several guidelines should be followed to enhance the performance of a harvester when designing the microstructures of piezo-composites. First, the height-to-width aspect ratio of the piezoceramic pillars should be larger than 2; this is because a half-wave transverse vibration of the piezo-pillars that is much higher than the fundamental thickness mode is required so that the harmonics will not be coupled to the thickness vibration. Second, the resonant frequency of the stopband edge should be higher than twice the resonant frequency of the fundamental thickness mode. Consequently, the gap between the piezo-pillars ought to be smaller than $c_s/2f$, where f and c_s are the thickness resonant frequency of the piezo-pillars and the shear wave velocity of the filler (EPO-TEK 301 epoxy resin), respectively. According to the above theoretical analysis, 2–2 and 1–3 type F-KNN ceramic/epoxy piezo-composites with miniaturized piezo-pillars (80 μm in width) and kerfs (20 μm) were designed and fabricated (Fig. 2b–f). In addition, a matching layer made from silver-powder-loaded epoxy (Z_m: $\sim$6.3 MRayl) was added to compensate for acoustic impedance mismatch between the piezoelectric materials (for F-KNN, Z_P: $\sim$23.4 MRayl) and tissue (Z_a: $\sim$1.7 MRayl) (Fig. 2c, e, and f and Fig. S5, ESI†) and thus improve ultrasonic energy transmission (simulation results and design guidance are given in Fig. S6, ESI†). The final rigid piezo-element cured with a backing layer (305 μm; E-solder 3022) has a spatial volume of $\sim 1.5 \times 1.5 \times 0.5$ mm^3 (Fig. 2c and e). The as-fabricated piezo-elements exhibit a resonant frequency of about 14–17 MHz (Fig. 2g–i) and the longitudinal coupling coefficient k_{33} and voltage coefficient g_{33} were substantially augmented through the suppression of the shear vibrating modes, especially in the 1–3 type piezo-structure (*e.g.*, $k_{33} \approx 0.65$, $g_{33} \approx 40.1$ V m $N^{-1} \times 10^{-3}$) (Fig. 2j), ensuring the acoustic sensitivity and high output capabilities of the device. Some important acoustic and electrical parameters of the pure F-KNN ceramic and as-fabricated piezo-composites are summarized in Table 1.

Working principle of the PA and PU hybrid-induced energy transfer

The hybrid energy transfer strategy proposed in our work uses both PA and PU waves to carry the available energy. The process involves three main parts: acoustic excitation, transmission,

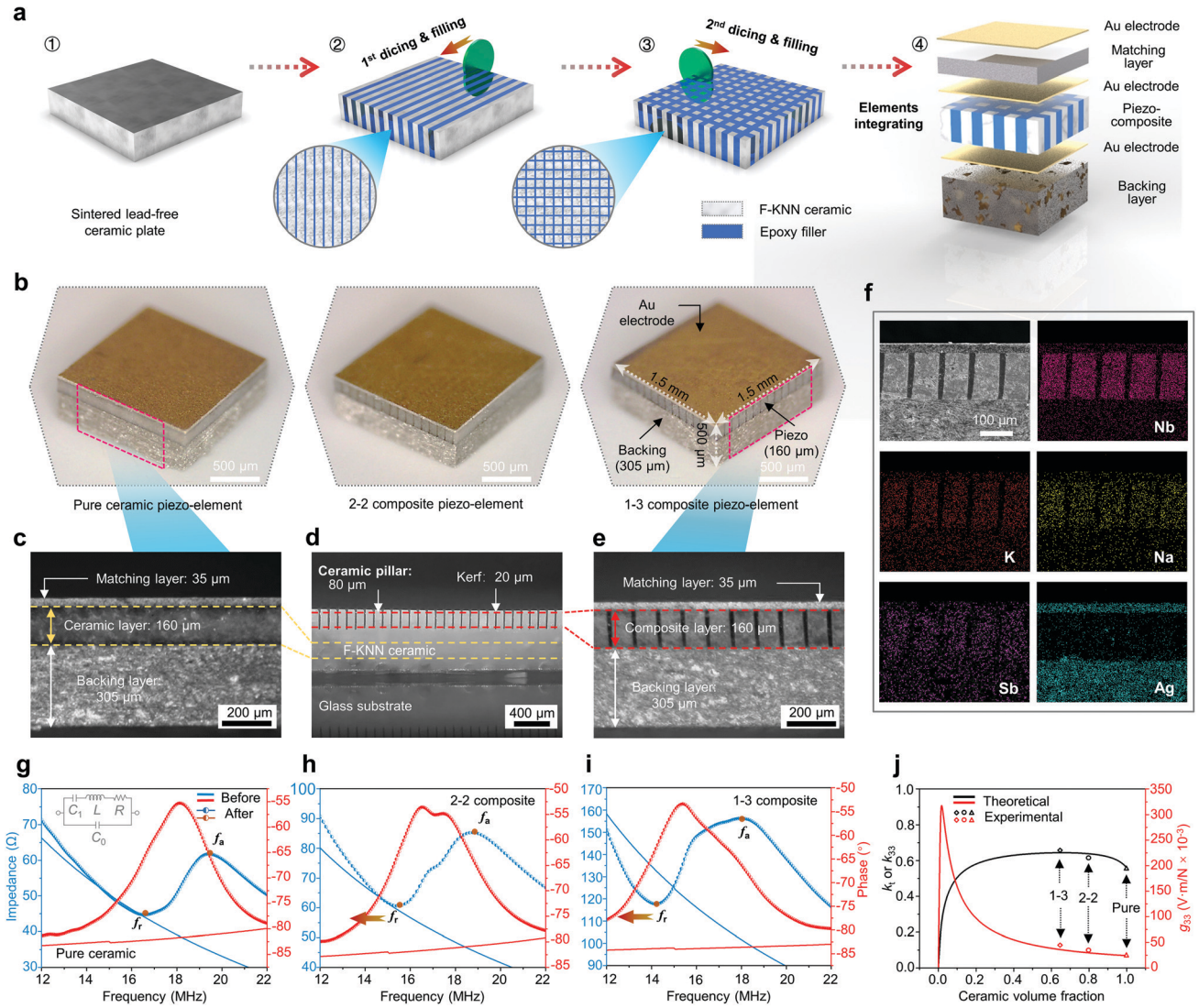

Fig. 2 Structural optimization and characterization of the piezo-elements. (a) Schematic diagrams showing the process of preparing the 2–2 and 1–3 ceramic/epoxy piezo-elements using a modified dicing-and-filling technique. (b) Optical images of the prepared three piezo-elements with a pure ceramic layer, a 2–2 composite layer, and a 1–3 composite layer. The overall size of each element is 1.5 × 1.5 × 0.5 mm^3. (c) An optical image showing the pure ceramic piezo-element, which is mainly composed of a matching layer (35 μm), a pure ceramic layer (160 μm), and a backing layer (305 μm). (d) An optical image showing the F-KNN ceramic pillar array after dicing. The width of each ceramic pillar is 80 μm and the kerfs are 20 μm. (e) An optical image showing the 1–3 composite piezo-element, which is mainly composed of a matching layer (35 μm), a 1–3 composite layer (160 μm), and a backing layer (305 μm). (f) Energy dispersive spectroscopy (EDS) elemental mapping of a 1–3 piezo-element. Impedance and phase angle spectra of (g) pure ceramic, (h) 2–2 composite, and (i) 1–3 composite piezo-elements before and after poling, demonstrating the wider resonance spectrum of the 1–3 composite piezo-element. The resonant (f_a) and anti-resonant (f_r) frequencies are labeled with shaded circles. The inset in (g) shows the equivalent *RLC* circuit diagram of the piezo-elements. (j) Electromechanical coupling coefficient (k_t or k_{33}) and piezoelectric voltage coefficient (g_{33}) values of the piezo-composites (symbols: experimental data; lines: theoretical predictions).

and reception. First, PU excitation is carried out based on a focused ring piezo-transducer that consists of a PZT piezoceramic plate with electrodes plated on both sides and that converts electricity into mechanical energy through the inverse piezoelectric effect (Fig. 3a).[41] Finite-element-analysis (FEA) simulations of the acoustic field distribution were performed for the piezo-transducer, as shown in Fig. 3b. Due to the focused ring architecture, the energy generated is focused into a small area through the confined wave beam, which not only improves the magnitude (~50 dB) and resolution of the acoustic excitation but also reduces energy dissipation caused by the divergence of the sound beam. Different from PU excitation, the PA excitation process typically starts when a short laser pulse is shined on a light-absorbing material (Fig. S7, ESI†). A composite made from graphene nanoplatelet (5 wt%)-loaded polydimethylsiloxane (GNPs–PDMS) was used in our work. As photons propagate in the composite, some are absorbed by the GNPs. The various absorption mechanisms involving the PA signal include (but are not limited to) vibrational absorption,[42] electronic absorption, surface plasmon

Table 1 The electrical and acoustic properties of the F-KNN ceramic and as-fabricated 2–2 and 1–3 piezo-composites

Specifications	F-KNN ceramic	2–2 composite	1–3 composite
Piezoelectric coefficient d_{33} (pC N^{-1})	471	451	430
Electromechanical coupling coefficient k_t or k_{33}	0.56	0.61	0.65
Relative free permittivity $\varepsilon_{33}^{T}/\varepsilon_0$ (at 1 kHz)	2200	1650	1210
Curie temperature T_C (°C)	250	N/A	N/A
Dielectric loss tan δ	0.03	0.02	0.02
Piezoelectric voltage coefficient g_{33} (V m $N^{-1} \times 10^{-3}$)	24.2	30.9	40.1
Thickness h (μm)	160	160	160
Density ρ (kg m^{-3})	4410	3730	3180
Resonant frequency f_r (MHz)	16.6	15.4	14.2
Anti-resonant frequency f_a (MHz)	19.4	18.7	18.0
Acoustic velocity c_p (m s^{-1})	5312	4928	4544

resonance absorption,[43] and stimulated Raman absorption.[44] The absorbed optical energy is partially or completely converted into heat through the nonradiative relaxation of the excited object (Fig. 3c).[45] The laser-induced pressure waves propagate as ultrasound waves and the acoustic pressure can be expressed as follows[46] (Note S1, ESI†):

$$\left(\nabla^2 - \frac{1}{v_s^2}\frac{\partial^2}{\partial t^2}\right)p(r,t) = -\frac{\beta}{C_p}\frac{\partial H(r,t)}{\partial t}, \quad (1)$$

where v_s is the acoustic velocity, C_p is the specific heat capacity, β is the volume expansion, and $H(r,t)$ is the heating function. Fig. 3d shows FEA simulations of the PA wave field distribution. When the GNPs–PDMS film received the Gaussian laser pulse, PA waves were generated from the surface of the film and propagated outward. The PA wave response strongly corresponds to the assigned parameters, such as the laser pulse energy and width, demonstrating the feasibility that this light-induced PA wave could be used for carrying out further PA-related energy transfer strategies.

For acoustic reception, piezoelectric materials are natural candidates for vibration-based energy harvesting. An equivalent circuit model for a piezoelectric energy harvester is shown in Fig. 3e. Both surfaces of the harvester have electrodes, and the electrodes are connected *via* a circuit with an impedance of Z_L. The upper surface of the device is driven by the time-harmonic surface normal stress T_{33}. Under an ultrasonic pressure load, the harvester vibrates along the thickness direction. The impedance Z_0 of the harvester can be determined as follows:[47]

$$Z_0 = -\frac{1}{i\omega C_0}\frac{\xi h\cot(\xi h) - {e_{33}}^2/\varepsilon_{33}\bar{C}_{33}}{\xi h\cot(\xi h)}, \quad (2)$$

where $C_0 = \frac{\varepsilon_{33}S}{2h}$, $\xi^2 = \frac{\rho\omega^2}{\bar{C}_{33}}$ and $\bar{C}_{33} = C_{33}\left(1 + \frac{{e_{33}}^2}{\varepsilon_{33}c_{33}}\right)$. C_0, C_{33}, ε_{33}, and e_{33} are the capacitance, effective elastic, dielectric, and piezoelectric constants, respectively. ω, ρ, and ξ are the angular frequency, density, and wavenumber, respectively. S and h are the area and thickness of the piezo-element. The total output voltage V is derived as follows:[47]

$$V = -\frac{Pk^2h}{e_{33}(1+k^2)}\frac{Z_L}{\xi h\cot(\xi h)(Z_0+Z_L)}, \quad (3)$$

where P is the ultrasound pressure applied to the piezo-element and k is the electromechanical coupling factor of the piezo-materials. Piezo-composite microstructures were therefore designed and fabricated to improve the output. The simulation results showing the piezo-potentials produced by the three piezo-elements are illustrated in Fig. 3f–h. The average piezo-potentials induced in the composites are much higher than in the pure ceramic due to the suppressed shear vibrating modes and augmented coupling coefficient k, especially in the 1–3 piezo-composite.

Output performance evaluation

To evaluate the output performances of devices fabricated from different piezo-elements, we measured the piezo-potentials induced by PU and PA waves. First, portable external sources are paramount for wireless power-supply systems. Fig. 4a presents the architecture of a focused ring ultrasound transducer (outer diameter: 28 mm, inner diameter: 10 mm, focal length: 25 mm) configured with an optical fiber (Thorlabs, Inc.), which serves as a hybrid acoustic source to provide transmittable ultrasound energy. Details about the experimental setup and method are shown in Fig. 4b and Fig. S8 (ESI†). In this basic performance test, both the twining LFEH device and the ultrasound transducer including an optical fiber were immersed in deionized water. In addition, a 320 μm flexible GNPs–PDMS film patch (Fig. 4c) as a photoacoustic converter was laminated onto the device surface; this absorbs the pulsed laser to generate photoacoustic energy, directly inducing the piezo-elements (detailed descriptions are given in the Experimental section).

The three LFEH devices fabricated from pure ceramic, 2–2 composite, and 1–3 composite piezo-elements generated open-circuit (OC) voltages of 1.12, 1.74, and 2.02 V_{pp} (Fig. 4d), respectively, under PU induction with a frequency of 3.3 MHz and an input voltage of 100 V_{pp} (the generated PU pressure was ~3.39 MPa). As expected, the generated voltage is much higher when using the 1–3 composite elements as a result of the substantial augmentation of the longitudinal coupling coefficient k_{33} and voltage coefficient g_{33} (Fig. 2j and 3h). A similar output voltage trend was observed in the PA-induced results. Using a trigger current of 4 A (~182 μJ per laser pulse), the measured OC voltages are 0.31, 0.43, and 0.60 V_{pp}, respectively, for pure ceramic, 2–2 composite, and 1–3 composite devices (Fig. 4e). Additionally, the waveform of the PA-induced output signal is a typical short pulse with a center frequency of about 1.0 MHz (Fig. 4e (right panel) and Fig. S9, ESI†), indicating that the output signals are produced during PA wave propagation and not as a result of other interference. In order to distinguish the PU- and PA-induced signals, the tunable PU cycle number was set to 100 (Fig. 4d and Fig. S10, ESI†). A plot of the PU and PA hybrid-induced signals is shown in Fig. 4f. The PU and PA pulse repetition frequency (PRF) values are both set to 1 kHz, and the PA signal is delayed by 0.5 ms. Compared to a PA-induced short pulse, the PU-induced signal possesses a wide waveform (100 cycles) with a typical reflection and ringdown phase (Fig. 4f (right panel)), demonstrating blurred time resolution but also that more usable energy can be carried in a single PU

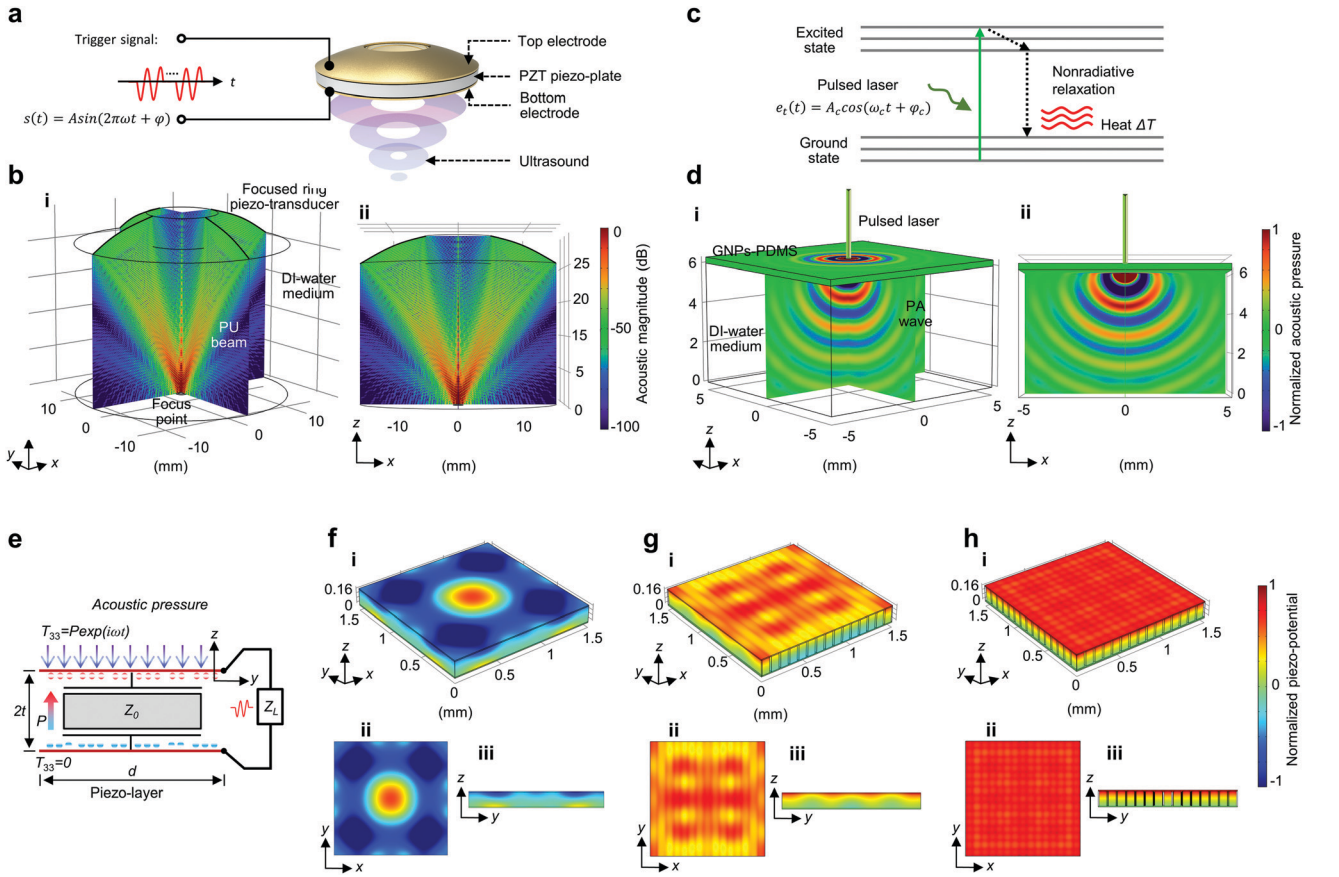

Fig. 3 The principles and simulations of PA and PU hybrid-induced energy transfer. (a) A schematic diagram illustrating the major concept of a PU transducer. (b) A simulated PU field generated by a focused ring piezo-transducer with an inner diameter of 10 mm, an outer diameter of 28 mm, a focal length of 25 mm, and a center frequency of 3.3 MHz, showing a spatially confined wave beam. The color bar indicates the acoustic magnitude (from −100 to 0 dB) calculated *via* the formula $20\log|P(x,y,z)|$. P is the acoustic pressure. (c) A schematic diagram illustrating the major concept of PA excitation. (d) A simulated PA field generated from 320 μm GNPs–PDMS film irradiated with a pulsed laser. The color bar indicates the normalized acoustic pressure. (e) The equivalent circuit model for a piezo-element induced by an acoustic field. Simulated piezo-potential distributions inside (f) pure ceramic, (g) 2–2 composite, and (h) 1–3 composite piezo-elements induced by the same acoustic field. A higher average potential distribution is achieved in the 1–3 composite element since the shear vibration modes in the x–y direction are suppressed. The color bar indicates the normalized piezo-potential.

pulse upon increasing the repetition cycles (Fig. S11, ESI†). Therefore, PU induction is suitable for continuously charging implants.[9] The PA signal with high spatial–temporal resolution and a short pulse length (∼2 μs) is more advisable for fine neurostimulation and signal communication *via* modulating the incident pulsed laser.[17,21] More interestingly, owing to its outstanding mechanical compliance and light weight (Fig. 4c), the GNPs–PDMS film patch can maintain intimate and stable contact with the target object (*e.g.*, human skin) both mechanically and acoustically. The combination of a flexible patch and a fine optical fiber provides a portable, lightweight, and high-resolution acoustic source outside the body for use in wireless transmission systems. On the one hand, the presence of the patch loaded with GNPs enhanced the light absorption characteristics to promote PA excitation, thus obtaining outstanding PA output. The fundamental vibration frequency of the GNPs–PDMS film can be expressed as $f = \frac{c}{4l}$,[26] where c is the acoustic velocity and l is the thickness of the patch. 1.0 MHz ultrasound was detected from the 320 μm GNPs–PDMS film through the fast Fourier transform (FFT) of the output signal (Fig. S9, ESI†). We also evaluated the laser-induced PA output without a GNPs–PDMS film patch and an inferior signal was observed. On the other hand, the GNPs–PDMS film patch will not significantly affect the PU propagation due to its acoustic impedance being similar to water and tissue. During PU-induced tests, the output voltages showed only slight attenuation (<7%) (Fig. S12, ESI†). The excellent performance of the GNPs–PDMS film patch in both PA- and PU-induced tests is attributed to its outstanding mechanical, optical, thermal, and acoustic properties, guaranteeing the realization of efficient hybrid energy transfer and having great potential for future portable and multifunctional medical applications.

The frequency relationship between the output voltage of the device and the PU frequency was also evaluated. As mentioned above, the LFEH array is an ultrasonic receiver that converts sensed acoustic pressure into electricity. Receiving in this case is a non-resonant process that performs well over a wide frequency range that is lower than the resonance frequency (*e.g.*, the

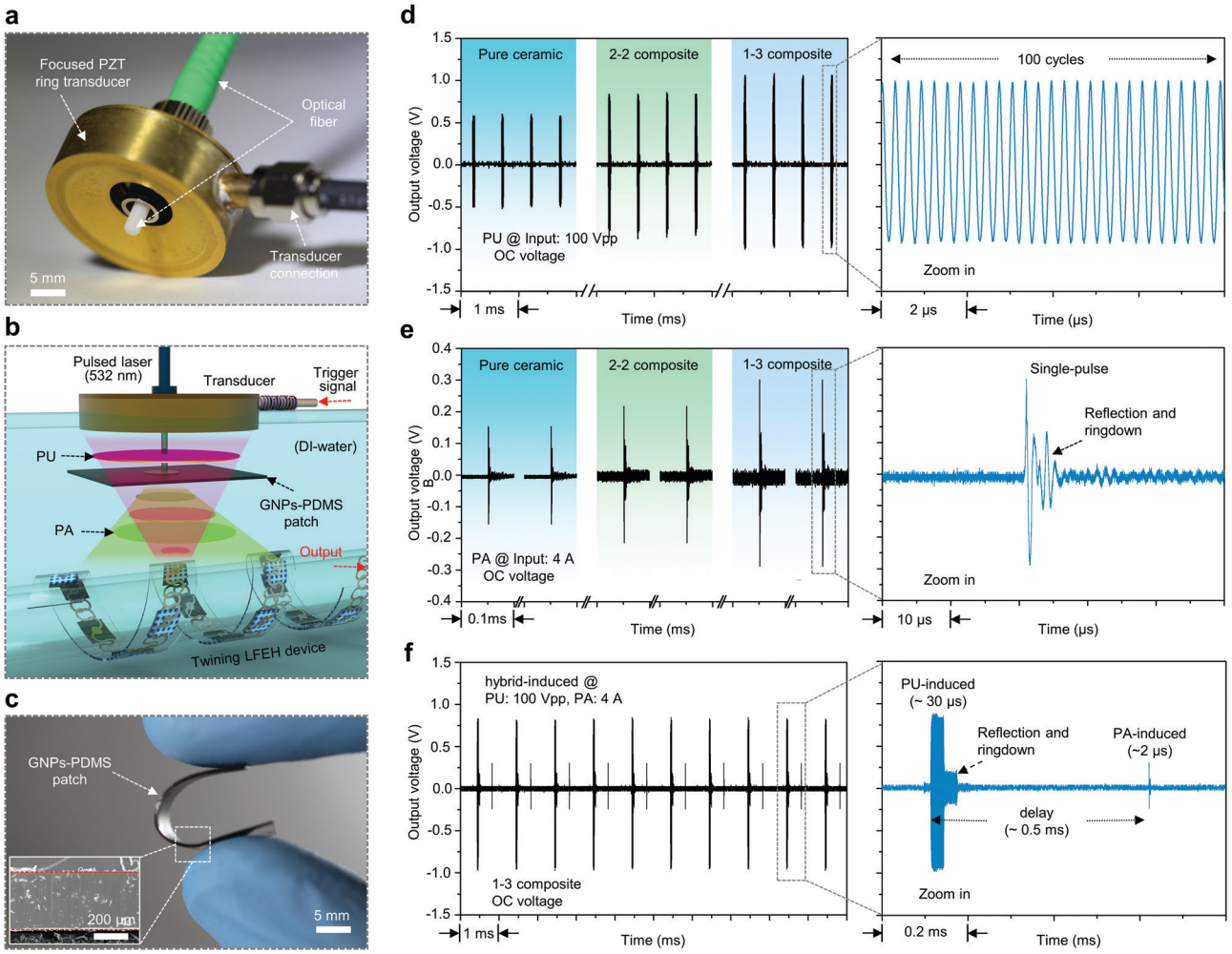

Fig. 4 The effects of material structure on output performance. (a) An optical image showing the focused ring piezo-transducer configured with an optical fiber. (b) A schematic illustration of the process of PU and PA hybrid-induced energy transfer. (c) An optical image of the flexible GNPs–PDMS patch; inset: a cross-sectional SEM micrograph of the patch. (d) PU induction: the output voltage amplitudes of LFEH devices fabricated with three piezo-structures. (e) PA induction: the output voltage amplitudes of LFEH devices fabricated with three piezo-structures. (f) PU and PA hybrid-induction: output voltage amplitudes of the LFEH device fabricated with 1–3 composite elements. For the PU induction mode, the trigger signal was set as follows: cycle number, 100; frequency, 3.3 MHz; PRF, 1 kHz. For the PA induction mode, the trigger signal was set as follows: laser wavelength, 532 nm; pulse width, 5–100 ns; PRF, 1 kHz; delay, 0.5 ms compared with PU. All output signals were directly measured using a digital oscilloscope without any amplification.

resonance frequency of our 1–3 piezo-element is 14.2 MHz).[48] Different from the ultrasonic receiving mode and PA excitation induced by a laser pulse, PU excitation is a resonant mode that directly converts electrical energy to mechanical energy, and optimal conversion efficiency is achieved when operating near the resonant frequency. The output voltage amplitudes of the 1–3 composite LFEH device were therefore measured over a wide frequency range (2–4 MHz). The maximum voltage was obtained at 3.3 MHz, corresponding to the resonance frequency of the focused ring piezo-transducer (Fig. S13, ESI†). This result is consistent with the pulse-echo response testing of the piezo-transducer itself (Fig. S14, ESI†), demonstrating the accurate identification of ultrasonic frequencies by the LFEH device when acting as an acoustic harvester. Energy transfer was also performed in saline water and porcine blood to verify the ability of the LFEH device to operate in the body (Fig. S15, ESI†).

Applications for wirelessly powering electronics

To use the LFEH device as a wireless power supply in implantable devices, it is necessary to realize sufficient electric power from the emitted ultrasonic waves and deliver or store the generated electricity. The instantaneous power of the LFEH device was therefore investigated *via* measuring the output voltage amplitudes under various external loads ranging from 25 Ω to 10 kΩ, as shown in Fig. 5a. With increasing resistance, the output voltage amplitudes increase gradually before saturating under higher external loads. The corresponding instantaneous output power densities were estimated. When the load Z_L is equal to the internal electrical impedance Z_0 of the LFEH device, the maximum power consumed in the load is reached.[47] Fig. 5b shows the instantaneous power densities of the LFEH device in response to diverse resistive loads, yielding optimal values of 103.1 mW cm^{-2} and 7.5 mW cm^{-2} near 150 Ω for PU

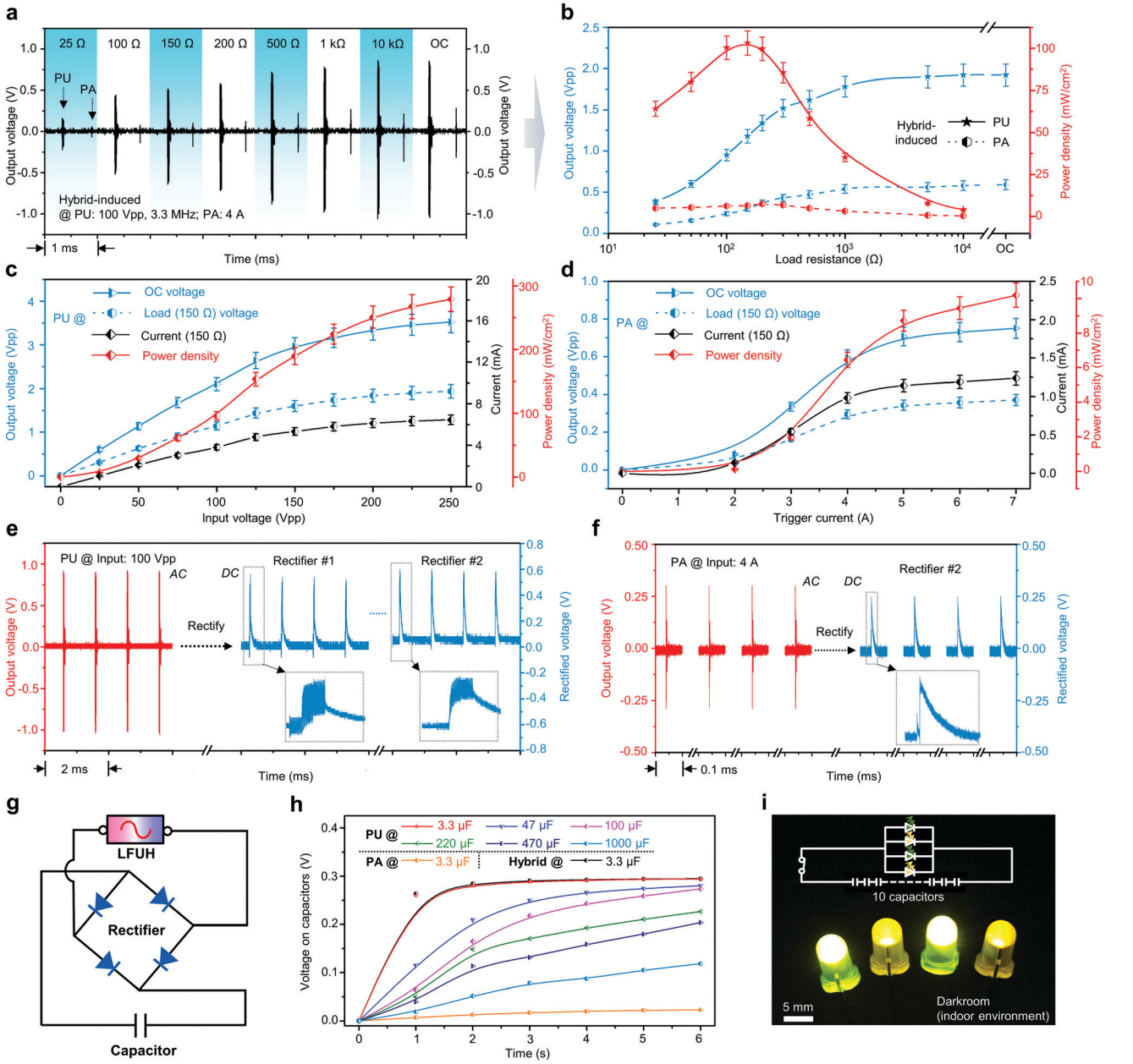

Fig. 5 Applications of the LFEH device. PU and PA hybrid-induction: (a) output voltage amplitudes and (b) corresponding power densities of the LFEH device in response to diverse loads, showing optimal outputs near 150 Ω. (c) PU induction: output voltage amplitudes and calculated corresponding currents and power densities (at 150 Ω) from the LFEH device using different trigger voltages. (d) PA induction: output voltage amplitudes and calculated corresponding currents and power densities (150 Ω) from the LFEH device using different trigger currents. The output rectification of the device during (e) PU and (f) PA induction. (g) A schematic illustration of the LFEH device connected to a rectifier and rechargeable capacitor. (h) Voltages across capacitors as a function of time during charging with the LFEH device *via* PU and PA induction. (i) An optical image showing 4 commercial LEDs connected in parallel and lit up using the electricity stored in the capacitors.

and PA induction, respectively. Considering the repetition period, the corresponding root mean square (RMS) power densities were calculated to be 1.55 mW cm^{-2} for PU induction and 3.75 nW cm^{-2} for PA induction. Although the RMS values are lower than the instantaneous ones, they can be improved *via* increasing the duty cycle for practical applications (Fig. S11, ESI†). According to eqn (2), piezoelectric harvesters generally have lower internal impedance during high-frequency operation.[49] The acoustic frequency used in this work is at the megahertz level, which is much higher than the kilohertz-level ultrasonic frequencies used in previously reported works.[9,12,16,50] Therefore, compared to traditional piezoelectric and triboelectric generators with internal electrical impedance at the megaohm level,[51–54] the high-frequency (megahertz-level) operation mode enables our device to obtain extremely low internal electrical impedance (~150 Ω), significantly

improving the output power of the device. Further evaluation was performed *via* testing the input dependence of the output. The output voltages increased and tended to saturate in response to increasing input settings, as shown in Fig. S16 and S17 (ESI†). The maximum OC voltages were 3.52 V_{pp} for PU induction and 0.75 V_{pp} for PA induction. The corresponding currents and load power densities at 150 Ω were also calculated, as shown in Fig. 5c and d. Instantaneous power densities of up to 278.8 and 10.2 mW cm^{-2} can be achieved in PU and PA operation modes, respectively, showing that the excellent output capabilities of our hybrid-induced device outperform most ultrasound-induced wireless energy harvesters (Table S1, ESI†).[9,12,13,31,50]

Two applications are demonstrated next to show that the hybrid-induced device could wirelessly provide power: charging up capacitors and lighting up a commercial LED array. Alternating current (AC) signals are first rectified into ordinary direct current (DC) signals *via* a pre-designed full-wave bridge rectifier circuit so that they are compatible with general electronics (Fig. 5g). Owing to the high-frequency (≥1 MHz) characteristics of the output signals, two rectifiers were separately tested in the pre-designed circuit to control the quality of the rectified DC signals. One is a commercial silicon bridge rectifier (#1) (Cylewet CYT1014) and the other is a rectifier (#2) composed of four Schottky barrier rectifier diodes (BOJACK SR560) (Fig. S18, ESI†). Due to the fast recovery time (~ps) of Schottky diodes,[55] the rectified signals exhibit less disturbance (Fig. 5e and f). Capacitors with different capacitance values were then successfully charged, as shown in Fig. 5h. For example, a 3.3 μF capacitor was charged by our device to 23 mV in 6 s under PA induction. In contrast, a voltage of up to 0.28 V was obtained in 6 s for a 47 μF capacitor under PU induction. The average charging power $\bar{P}$ can be estimated in this process *via* the formula $\bar{P} = \frac{C_S V^2}{2t}$, wherein V is the increased voltage, t is the charging time, and C_S is the capacitance. Consequently, the energy stored in the capacitors increased by 0.9 nJ and 1.84 μJ in 6 s for the above PA and PU processes, indicating that the average charging capabilities are approximately 0.17 and 307 nW, respectively. The relatively low value obtained in the PA-induced process is mainly due to the lower duty cycle with a short-temporal-pulse PA signal (~2 μs per pulse). Therefore, the results further show that the PU-induced process with high output capabilities is more suitable for the continuous charging of implant batteries while the PA signal with high temporal resolution is more advisable for fine neurostimulation and signal communication. As demonstrated in Fig. 5i, the electrical energy generated from the LFEH device was successfully used to light up an array of four commercial light-emitting diodes (LEDs) *via* connecting ten charged capacitors in series, demonstrating the great potential of this system as a wireless power supply for implantable medical systems.

Ex vivo characterization in porcine tissue

Because the aim of this study was to develop a hybrid-induced wireless energy system for electronic transcutaneous multifunctional implants, we characterized the 3D twining LFEH device under porcine tissue (Fig. 6a–c), which is comparatively similar to human skin in terms of its composition and anatomy. *Ex vivo* characterization studies were also performed from multiple angles. Fig. 6c shows the *ex vivo* experimental setup, where the flexible GNPs–PDMS film patch was attached to the top surface of the porcine tissue sample and the LFEH device under the porcine tissue was wrapped around a soft silicone pipe that was connected to a rotating motor. First, the LFEH device was characterized under different thicknesses of skinned porcine tissue (Fig. 6d and e and Fig. S19, ESI†). At 5 mm, the LFEH device produced OC voltage amplitudes of more than 1.23 V_{pp} and 130 mV_{pp} (Fig. 6d and e) under PU and PA induction, respectively, which are ~61% and 23% of the values in the non-implanted case. The corresponding load (150 Ω) power densities are ~35.1 mW cm^{-2} and 313 μW cm^{-2} (Fig. 6f and g). The decreases in voltage and power are due to the dissipation of the acoustic waves caused by the absorption, reflection, and divergence of the wave beam in the different media and layered structures (Note S3, ESI†). The focused PU emission with a confined wave beam, therefore, exhibits a lower attenuation rate than the PA wave (Fig. 3a and b). Considering that different individuals possess varied thicknesses of skin, fat, and muscle, energy transfer in different biological tissue samples was also performed to verify the universality of the LFEH device (Fig. S20, ESI†). For example, the LFEH device under 12 mm of layered tissues, including skin, fat, and muscle, produced voltage amplitudes of about 910 mV_{pp} and 80 mV_{pp} under PU and PA induction (Fig. 6d and e), respectively. The corresponding power levels generated, approximately 21.3 mW cm^{-2} and 67 μW cm^{-2}, are still sufficient to charge the batteries of some small bioimplants (*e.g.*, pacemakers that consume ~1 to 100 mW) and to directly power electrical neurostimulators (consuming ~1 μW to 25 mW) and microscopic robots (consuming ~10 nW).[9,56] Additionally, the signal-to-noise ratio (SNR) of the PA-induced OC signal was calculated to be 22.5 dB in this 12 mm implanted case (Fig. 6e). If the emitted control signal is modulated by the digits "0" and "1", so-called amplitude-shift keying (ASK) modulation,[13] digital information can be transmitted *in vivo via* the ultrasound-induced link. Based on this working mechanism, programmable pulse tests were also performed *ex vivo via* the PU- and PA-induced process to demonstrate the potential of the LFEH device for use in signal communication (Fig. 6h). The trigger signal was programmed using pulse signals with one cycle. The length of a one-bit signal is 10 μs. Both the PU- and PA-induced signals are consistent with the programmed arrangement of the trigger signal in the time sequence. However, although the trigger pulse is set with one cycle, the PU-induced signal possesses a wider waveform with a lengthy reflection and ring-down phase (~8 μs), yielding blurred time resolution. The PA-induced signal with a short pulse length (~2 μs) therefore has more potential for signal communication when high temporal resolution is required. In Fig. 6i, we demonstrate the transmission of a two-dimensional image with an A-shape *via* PA-induced wireless communication. Each pixel is represented by binary code.

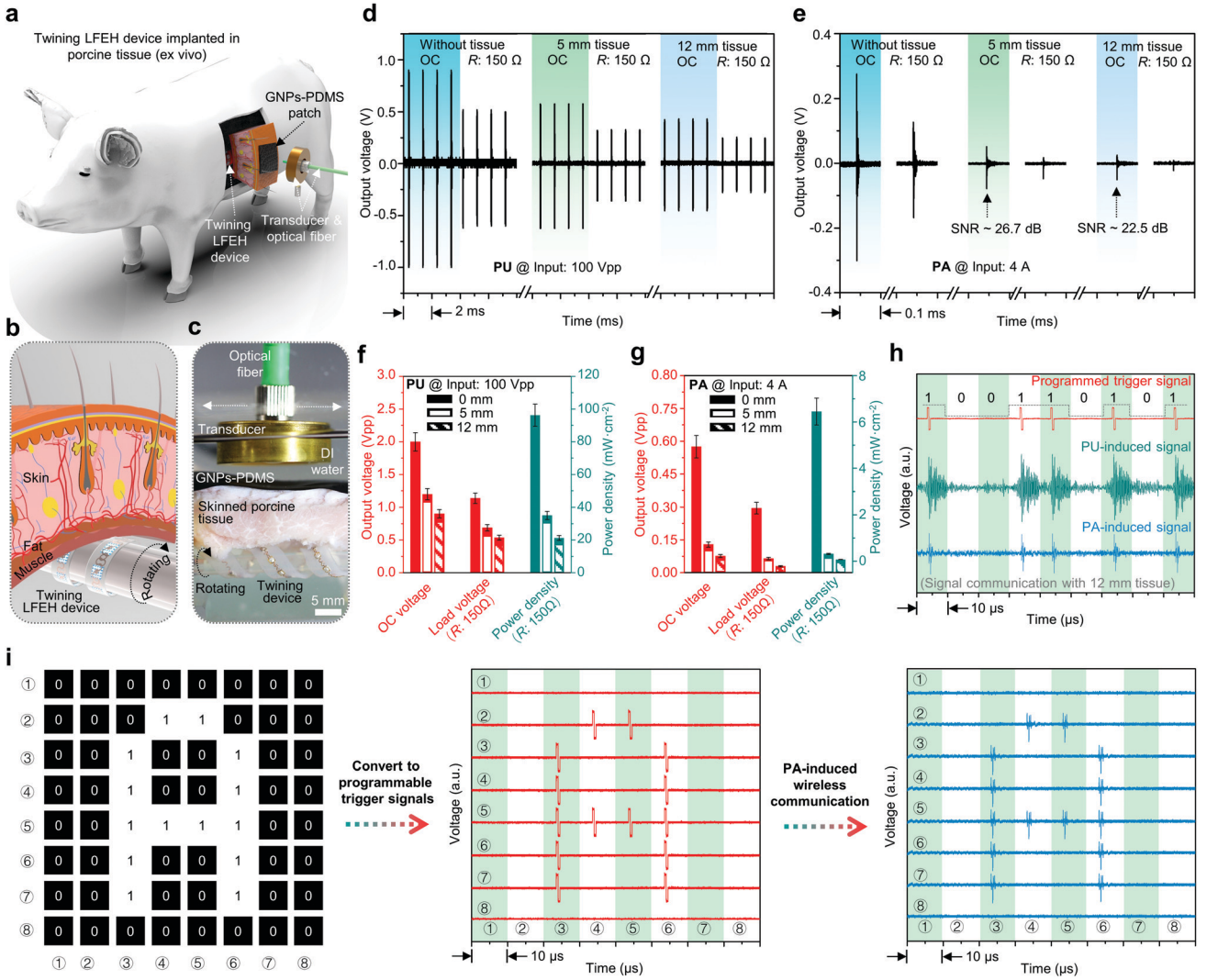

Fig. 6 The *ex vivo* characterization of wireless powering and communication in porcine tissue. Schematic diagrams of (a) the *ex vivo* porcine model and (b) skinned tissue showing the implanted 3D twining LFEH device. (c) An optical image showing the testing setup with the twining LFEH device implanted under skinned porcine tissue for PU and PA hybrid induction. The tissue surface is covered with a GNPs–PDMS patch and the LFEH device is wrapped around a soft silicone pipe that is connected to a rotating motor. Output voltage amplitudes of the LFEH device implanted under tissue samples of different thicknesses from (d) PU and (e) PA induction. Comparisons of the output voltages and power densities of the LFEH device characterized in porcine tissue under (f) PU and (g) PA induction. (h) The *ex vivo* characterization of signal communication performed *via* PU and PA induction. The trigger signal was programmed using pulse signals with one cycle. The length of a one-bit signal is 10 μs. (i) The transmission of a two-dimensional image realized through PA-induced wireless communication. Each pixel is represented by binary code and the output signals are decoded error-free in the time sequence.

At the output port, the measured signals can be decoded error-free in the time sequence, indicating that the PA-induced communication method is free of bit error and can be integrated with a transmission chip to achieve intelligent control in future applications. More interestingly, the PA-induced electrical outputs were still observed in the LFEH device without the GNPs–PDMS film patch attached to the tissue, showing that pure porcine skin tissue absorbed the pulsed laser to produce a PA signal. However, the signal magnitudes are several times lower than those in the presence of the GNPs–PDMS film (Fig. S21, ESI†), further explaining the importance of composite films with excellent optical, thermal, and acoustic properties for ensuring efficient PA energy conversion.

The 3D twining LFEH array was also tested *ex vivo* as an energy solution for multi-angle transmission *via* rotating the implanted device from 0 to 360 degrees using a connected motor, as shown in Fig. 6c. Acoustic receivers usually require special angles related to the sound beam to achieve optimal performance. The maximum ultrasound intensity is delivered to the harvester if the acoustic beam is perpendicular to the piezo-elements. Generally, the incident ultrasonic power will be weakened if the piezo-elements are tilted at an angle to the acoustic beam, as shown in Fig. 7a and b. Traditional harvesters are highly sensitive to the alignment, and they generally require well-arranged architectures to obtain a favorable angle. Therefore, the twining-plant-inspired array in our work possesses

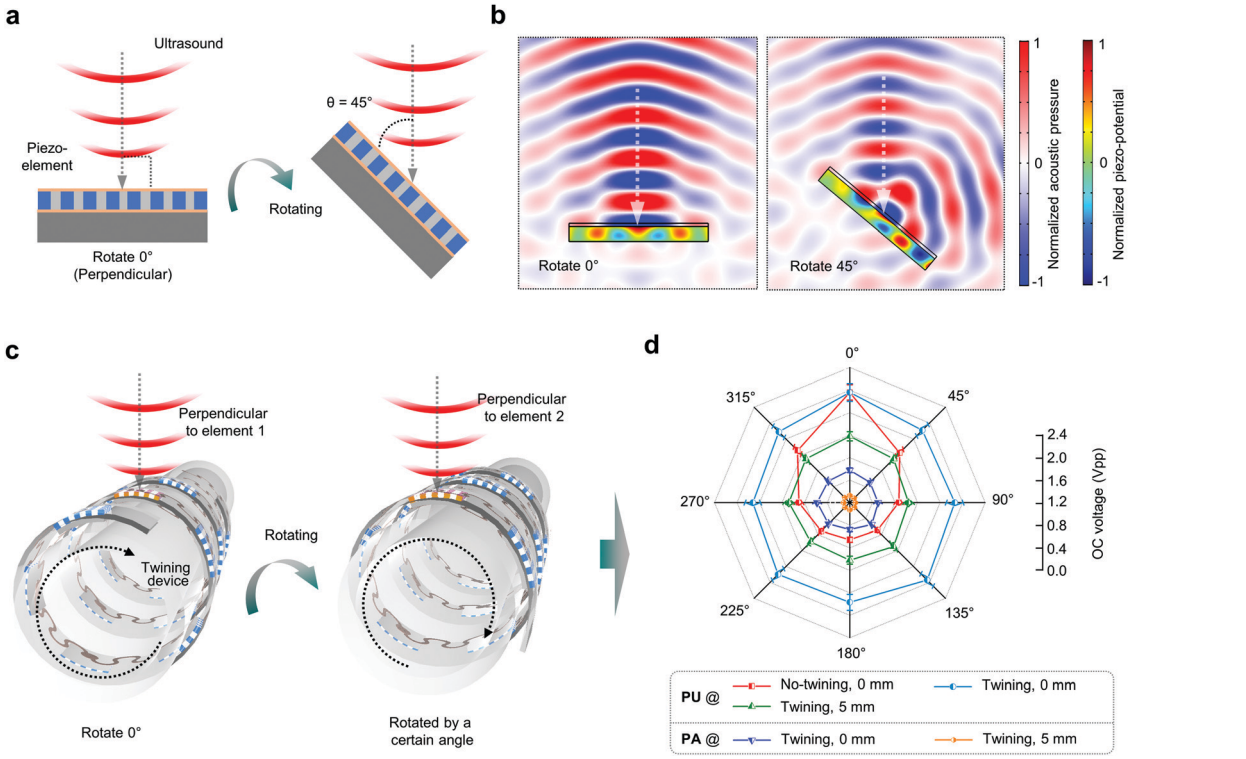

Fig. 7 The *ex vivo* characterization of multi-angle transmission. (a) A schematic diagram of ultrasound waves incident on a piezo-element from different angles. (b) Simulated piezo-potential distributions inside a piezo-element under ultrasonic induction at different incident angles. A reduced average piezo-potential is observed from the tilted piezo-element. (c) Schematic diagrams of the 3D twining device receiving ultrasound while rotating. (d) Output voltages of devices as a function of the rotation angle, showing the ability of the 3D twining device to harvest ultrasound from multiple angles.

a spiral configuration to maintain multi-angle coverage of the piezoelectric elements without losing the twining layout, even under movement (Fig. 7c). The results show obvious changes (>60%) in the output voltages in the non-twining case (Fig. 7d), especially when the array is rotated behind the pipe (180 degrees). In contrast, the device in the twining state exhibits only slight changes (<8%) during rotation (Fig. 7d). In this way, the spirally arranged piezo-elements can capture acoustic energy from multiple angles without sacrificing stability, even under large deformation and movement stress. The 3D twining LFEH device could also accommodate complex implantation in the human body *via* integration with stimulators, biosensors, and wireless signal actuation and transmission chips in the future.

Safety and further optimization

In this work, a PA and PU hybrid-induced energy transfer strategy was proposed *via* designing an architecture that combines an ultrasonic transducer, a fiber-photoacoustic converter, and an energy harvester. Although the reported LEFH device has demonstrated potential for use in implanted devices, the biocompatibility, ultrasound-related biological effects, and further optimization are worth discussing to promote its practical use.

Firstly, there are two main considerations in the selection of biocompatible materials for our LFEH device. On the one hand, a KNN-based lead-free piezo-composite, which possesses biocompatibility, environmental friendliness, and good electrical properties, was selected as the array element. KNN-based materials mainly contain the elements K, Na, and Nb, and they have been developed into the most promising lead-free piezo-materials to replace lead-based examples.[57] Additionally, several previous studies have proved the non-toxicity and biocompatibility of KNN-based piezo-materials in implantable devices.[33,35] On the other hand, silicone elastomer was used for encapsulation. Primarily due to the stability of Si–O–Si bonds, silicone elastomers are very suitable for medical implants in many aspects, because of factors such as their unsurpassed biocompatibility and hypoallergenic nature, bacterial resistance, long shelf life, and superior insulating properties. For over half a century, silicone elastomers have proven to be a safe material and have been used in long-term implants for decades.[58] Therefore, the selection of these materials ensures the biocompatibility of the LFEH device in the human body.

Secondly, some side-effects may occur when high-energy ultrasound waves propagate through organisms, such as thermal and mechanical effects. These effects result in a wide variety of tissue injuries, including abnormal cell migration, necrosis, altered gene expression, and membrane dysfunction.[59] Thus, high-energy ultrasonic waves combined with a longer exposure time may lead to detrimental results. To evaluate the mechanical damage, the mechanical index (MI) is usually specified, which is defined as follows:[15]

$$\mathrm{MI} = \frac{\mathrm{PNP}}{\sqrt{f_c}} \cdot \frac{\sqrt{1\ \mathrm{MHz}}}{1\ \mathrm{MPa}}, \quad (4)$$

where PNP is the peak negative pressure of ultrasound in MPa and f_C is the center frequency of ultrasound in MHz. High-frequency excitation, on the one hand, can reduce the internal resistance of the device, thereby increasing the power (Fig. 5b), and on the other hand, it can reduce mechanical damage. As recommended by the U.S. Food and Drug Administration (FDA), the MI for general ultrasound diagnostic systems should not exceed 1.9. Combining eqn (4) and ultrasonic pressure tests using a hydrophone (Fig. S22, ESI†), the MI is calculated to be 1.87 for the 3.3 MHz PU waves ($\sim$3.39 MPa) under an excitation voltage of 100 V_{pp} and 0.74 for the 1.0 MHz PA waves ($\sim$0.74 MPa) under an excitation current of 4 A, which are below the safety threshold. For ultrasound-related thermal effects, the thermal index (TI) is specified and defined as follows:[60]

$$\mathrm{TI} \equiv \frac{W_p}{W_{deg}} = \frac{\min\left(W, I_{spta}\ 1\ \mathrm{cm}^2\right) \cdot f}{210\ \mathrm{mW\ MHz}}\ (\text{in soft tissue}), \qquad (5)$$

where W_p is the derated acoustic power at the depth of interest and W_{deg} is the estimated power necessary to raise the tissue equilibrium temperature by 1 °C according to a chosen specific tissue model. For the 3.3 MHz PU waves used in the experiments (cycle number: 100; PRF: 1 kHz; excitation voltage: 100 V_{pp}), the TI is calculated to be 0.458, which is considered to be very safe by the British Medical Ultrasound Society.[61] PA waves with a lower intensity and lower frequency have a smaller TI. Considering general implantable applications, therefore, pulsed waves with a duty cycle as low as possible are recommended for energy transfer.

Thirdly, a GNPs–PDMS patch was designed and exploited to assist PA generation; this not only enhanced the output of the PA signal but also acted as a protective layer to block the direct pulsed laser irradiation of tissue. In future investigations, the conversion of photoacoustic energy might be further optimized through aligning GNPs in the PDMS matrix,[26] and the acoustic-electric coupling performance of piezo-active materials could be further enhanced through composition and structural design. If the conversion efficiency is significantly improved, organisms can be studied at lower intensities and the biological effects of ultrasound can be minimized.

Last but not least, this work only focused on the design and manufacture of an implantable LFEH device, without considering in too much detail the electric circuits and other applications. Wireless signal actuation and transmission chips can be integrated into this wireless energy transfer system to achieve diverse uses and functions in future work, such as in smart implantable/wearable devices for healthcare and motion monitoring, portable/mobile electronic devices for wireless powering and data transmission, home automation for switches and smart metering, and intelligent automobile systems for machine health monitoring and wireless sensing.[11,14,62]

Conclusions

We have presented a new hybrid-induced energy transfer strategy that employs a delicate architecture configured with a focused piezo-transducer and a portable fiber-photoacoustic converter serving as the hybrid acoustic source to offer multimodal transmittable ultrasound energy for wireless multifunctional implants, adding a new dimension to bioelectronics. The prototype exploits a flexible design and strategic material integration to achieve safe and stable multifunctionality, combining PA- and PU-induced characteristics, and it has the merits of both high output power and high spatial–temporal resolution. The capability for wireless transfer through water, blood, and porcine tissue media was demonstrated. Following FDA regulations, the demonstrated LFEH device can generate a stable output in the order of milliwatts ($\sim$21.3 mW cm^{-2}) and allow high-resolution signal communication (SNR $\sim$22.5 dB) *ex vivo* under 12 mm-thick porcine tissue. Due to the unique device design with a thin profile and flexible mechanical properties, the array device allows 3D twining on the target surface, achieving energy capture from multiple angles without cumbersome operational procedures. Future research will focus on optimizing the system structure and performance *via* exploring the integration of more acoustic components, high-performance and biodegradable active elements, and wireless information transmission and actuation chips to create efficient, safe, controllable, and communicable wireless systems.

Experimental

Fabrication of the lead-free piezo-composite elements

(i) The Fe_2O_3-containing (K,Na)(Nb,Sb)O_3–(Bi,Na)ZrO_3 (abbreviated as F-KNN) lead-free piezoceramic was synthesized first *via* a solid-state sintering process. Bi_2O_3 (99.999%), Fe_2O_3 (99%), K_2CO_3 (99.0%), Na_2CO_3 (99.8%), Sb_2O_3 (99.99%), Nb_2O_5 (99.5%), and ZrO_2 (99.0%) were used as the raw materials. (ii) Second, a dicing-and-filling process (Tcar 864-1, Thermocarbon) was applied to fabricate the ceramic/epoxy piezo-composite, with a ceramic pillar width of 80 μm and kerfs of 20 μm. Insulating polymer (EPO-TEK 301 epoxy resin) was employed to fill the kerfs. (iii) Next, the fabricated piezoelectric samples were lapped down to 160 μm and sputtered with Au (100 nm) electrodes on both sides *via* a sputtering process (NSC-3000 Sputter Coater, Nano-Master). Materials that acted as the matching layer (35 μm) (silver-powder-loaded epoxy) and as the backing layer (300 μm) (E-Solder 3022) were cured separately on the top and bottom sides of the sputtered piezoelectric samples, as illustrated in Fig. S23 (ESI†). (iv) Then, the entire acoustic stack was diced into small pieces with a spatial volume of 1.5 × 1.5 × 0.5 mm^3. (v) Lastly, poling of the piezo-elements was implemented at 3 V μm^{-1} (d.c.) for 15–20 min. The same process outlined above was used for the preparation of pure ceramic, 2–2 composite, and 1–3 composite piezo-elements.

Fabrication of the twisting LFEH array

The whole fabrication process can be briefly summarized in three steps: (i) flexible electrode design and fabrication; (ii) assembling with active elements; and (iii) encapsulating. The process is initiated with the design of electrodes based on the

wavy structure and flexibility that the device is expected to achieve. A lathe (SD 400, PRAZI) was employed to equidistantly wind copper wire with a diameter of 100 μm on a 500 μm-diameter stainless-steel rod. The straight "spiral structure" was then removed from the rod and was pressed into a flat plane using a polished cube to obtain soft wavy-shaped electrodes. Next, an array with 13 piezo-elements was suitably arranged on a glass slide bonded with water-soluble tape (3M). The top and bottom electrodes were assembled separately with the piezo-components using solder paste (E-Solder 3022). Silicone elastomer (Ecoflex 00-30) was filled into the gaps to encapsulate the sandwiched device after plasma cleaning. The glass slides were then removed after 4 h after the elastomer was fully cured at room temperature, generating a freestanding flexible harvester array.

Fabrication of the focused ring transducer

The structural dimensions of the focused ring piezo-transducer were designed and optimized first based on PZT-5H ceramic with the Krimboltz, Leedom, and Mattaei (KLM) equivalent circuit based modeling software PiezoCAD. The designed PZT ring plate with the optimized dimensions of a thickness of 580 μm, an inner diameter of 10 mm, an outer diameter of 28 mm, and a focal length of 25 mm was then custom made by Del Piezo Specialties, LLC (Fig. S24, ESI†). The PZT ring plate with silver electrodes on both sides was then installed into brass housing. A subminiature version A (SMA) connector was connected with the back electrode using a wire. An Au (100 nm) electrode was sputtered across the front electrode and the brass housing to form a common ground connection. Lastly, 30 μm-thick parylene was deposited onto the whole external surface of the transducer as a protective layer.

Fabrication of the GNPs–PDMS film patch

First, 5 wt% of the graphene nanoplatelets (25 μm particle size, surface area 120–150 $m^2\ g^{-1}$) (Sigma-Aldrich) was poured into a PDMS matrix (containing a curing agent at a ratio of 0.1) (Sylgard 184, Dow Corning). The GNPs–PDMS composite was then spin-coated at 1500 rpm onto a glass substrate. The thickness of the spin-casted GNPs–PDMS film is about 320 μm. The curing process was done in a dry oven for 4 h at 80 °C. The cured GNPs–PDMS layer was diced into pieces of $0.8 \times 3.0\ cm^2$ in size and then peeled from the substrate. The process is illustrated in Fig. S25 (ESI†).

Materials characterization

The crystal structure of the synthesized F-KNN ceramic was evaluated *via* X-ray diffraction (XRD, DX2700). Field-emission scanning electron microscopy (FE-SEM, JSM-7500) was used to determine the surface morphology along with energy dispersive spectroscopy (EDS) studies. Side-view photos of piezo-elements were instantly taken after optical microscopy testing (SZ61, Olympus). The piezoelectric coefficient d_{33} was measured using a d_{33} meter (YE2730A, APC Products). The impedance spectra were analyzed using an impedance analyzer (4294A, Agilent). An inductance–capacitance–resistance digital bridge instrument (1715 LCR, QuadTech) was used to determine the capacitance. Based on the IEEE standard on piezoelectricity,[63] the acoustic and electrical properties of the F-KNN ceramic and the as-fabricated 2–2 and 1–3 type piezo-composites were calculated *via* the following equations:

$$\frac{\varepsilon^{T}}{\varepsilon_0} = \frac{C^{T}h}{\varepsilon_0 A}, \tag{6}$$

$$g_{33} = \frac{d_{33}}{\varepsilon_{33}^{T}}, \tag{7}$$

$$k_t \text{ or } k_{33} = \sqrt{\frac{\pi f_r}{2 f_a} \tan\left(\frac{\pi}{2}\frac{f_a - f_r}{f_a}\right)}, \tag{8}$$

$$c_p = f{\cdot}\lambda = 2 f_r{\cdot}h, \tag{9}$$

$$Z_a = \rho{\cdot}c_p. \tag{10}$$

FEA simulations

Finite element analysis (FEA) simulations were conducted using COMSOL (COMSOL Multiphysics 5.3a) to simulate the acoustic field distributions of PU and PA waves and the piezoelectric potential distributions in elements under ultrasound excitation. In simulations, the considered physics fields include pressure acoustics (frequency-domain), electrostatics, and solid mechanics, as well as the coupled interfaces of the piezoelectric effect and acoustic-structure boundary. The material parameters were set according to supplier datasheets or experimentally measured results. The geometries of the components were strictly consistent with the designs.

Output performance characterization

The outputs of the LFEH device were measured using a multifunctional ultrasonic testing system (Fig. S8, ESI†). A focused ring transducer equipped with an optical fiber as the hybrid acoustic source was installed on a 5-axis motorized stage (Opto-Sigma). The LFEH device wrapped around a silicone pipe was fixed 25 mm away from the piezo-transducer. In basic performance tests, the flexible GNPs–PDMS film patch was attached to the surface of the LFEH device (Fig. 4b). In *ex vivo* tests, the GNPs–PDMS film patch was attached to the top surface of the inserted porcine tissue (Fig. 6c). The focused piezo-transducer was triggered *via* a sinusoidal pulse signal, which was generated using a function generator (AFG3252C, Tektronix) and then amplified (40 dB) with an amplifier. The laser was launched using a 532 nm laser system (PS-L08, Spectra-Physics) and guided into the optical fiber *via* a lens. The output voltages generated by the LFEH device were directly detected using an oscilloscope (TDS 5052, Tektronix) with an internal resistance of 1 MΩ. The acoustic pressures of the PU and PA waves were measured using a hydrophone probe (HGL-1000, ONDA).

Author contributions

L. J. and Q. Z. designed the research. L. J. synthesized the F-KNN lead-free ceramic. L. J., Y. Z., and Y. S. prepared the

microfabricated piezo-elements. L. J. conducted flexible device fabrication. L. J. and G. L. performed characterization and data analysis. G. L. performed physical modeling and simulations. R. L. contributed to the preparation of the focused ring transducer. L. J. wrote the manuscript. Q. Z., Y. Y., Y. C., M. S. H., and L. J. planned, supervised, and led the project. All authors provided active and valuable feedback on the manuscript.

Conflicts of interest

The authors declare no competing interests.

Acknowledgements

The work is supported by unrestricted funds from Research to Prevent Blindness to USC Roski Eye Institute. G. L. is supported by the Alfred E. Mann Innovation in Engineering Doctoral Fellowship. The authors gratefully acknowledge Jie Xing for her assistance with the materials characterization.

References

1 G. D. Sanders, M. A. Hlatky and D. K. Owens, *N. Engl. J. Med.*, 2005, **353**, 1471–1480.
2 S. K. Mulpuru, M. Madhavan, C. J. McLeod, Y.-M. Cha and P. A. Friedman, *J. Am. Coll. Cardiol.*, 2017, **69**, 189–210.
3 V. Salanova and R. Worth, *Curr. Neurol. Neurosci. Rep.*, 2007, **7**, 315–319.
4 M. A. Wood and K. A. Ellenbogen, *Circulation*, 2002, **105**, 2136–2138.
5 H. Aubert, *C. R. Phys.*, 2011, **12**, 675–683.
6 S. Xu, Y. Qin, C. Xu, Y. Wei, R. Yang and Z. L. Wang, *Nat. Nanotechnol.*, 2010, **5**, 366–373.
7 D. H. Kim, H. J. Shin, H. Lee, C. K. Jeong, H. Park, G. T. Hwang, H. Y. Lee, D. J. Joe, J. H. Han and S. H. Lee, *Adv. Funct. Mater.*, 2017, **27**, 1700341.
8 Y. Chen, Y. Cheng, Y. Jie, X. Cao, N. Wang and Z. L. Wang, *Energy Environ. Sci.*, 2019, **12**, 2678–2684.
9 R. Hinchet, H.-J. Yoon, H. Ryu, M.-K. Kim, E.-K. Choi, D.-S. Kim and S.-W. Kim, *Science*, 2019, **365**, 491–494.
10 Q. Zheng, B. Shi, Z. Li and Z. L. Wang, *Adv. Sci.*, 2017, **4**, 1700029.
11 L. Jiang, Y. Yang, Y. Chen and Q. Zhou, *Nano Energy*, 2020, 105131.
12 L. Jiang, Y. Yang, R. Chen, G. Lu, R. Li, J. Xing, K. K. Shung, M. S. Humayun, J. Zhu, Y. Chen and Q. Zhou, *Adv. Funct. Mater.*, 2019, **29**, 1902522.
13 C. Chen, Z. Wen, J. Shi, X. Jian, P. Li, J. T. Yeow and X. Sun, *Nat. Commun.*, 2020, **11**, 1–9.
14 D. K. Piech, B. C. Johnson, K. Shen, M. M. Ghanbari, K. Y. Li, R. M. Neely, J. E. Kay, J. M. Carmena, M. M. Maharbiz and R. Muller, *Nat. Biomed. Eng.*, 2020, **4**, 207–222.
15 T. L. Szabo, *Diagnostic ultrasound imaging: inside out*, Academic Press, 2004.
16 L. Jiang, Y. Yang, R. Chen, G. Lu, R. Li, D. Li, M. S. Humayun, K. K. Shung, J. Zhu, Y. Chen and Q. Zhou, *Nano Energy*, 2019, **56**, 216–224.
17 K. Kim, M. Vöröslakos, J. P. Seymour, K. D. Wise, G. Buzsáki and E. Yoon, *Nat. Commun.*, 2020, **11**, 1–12.
18 J. Yao, *Light: Sci. Appl.*, 2017, **6**, e17062.
19 Y.-H. Pao, *Optoacoustic spectroscopy and detection*, Elsevier, 2012.
20 L. V. Wang, *Photoacoustic imaging and spectroscopy*, CRC Press, 2017.
21 Y. Jiang, H. J. Lee, L. Lan, H.-a. Tseng, C. Yang, H.-Y. Man, X. Han and J.-X. Cheng, *Nat. Commun.*, 2020, **11**, 1–9.
22 L. V. Wang and S. Hu, *Science*, 2012, **335**, 1458–1462.
23 A. Taruttis and V. Ntziachristos, *Nat. Photonics*, 2015, **9**, 219–227.
24 S. Gottschalk, O. Degtyaruk, B. Mc Larney, J. Rebling, M. A. Hutter, X. L. Deán-Ben, S. Shoham and D. Razansky, *Nat. Biomed. Eng.*, 2019, **3**, 392–401.
25 Z. Chen, Y. Wu, Y. Yang, J. Li, B. Xie, X. Li, S. Lei, J. Ou-Yang, X. Yang and Q. Zhou, *Nano Energy*, 2018, **46**, 314–321.
26 J. Li, J. Xu, X. Liu, T. Zhang, S. Lei, L. Jiang, J. Ou-Yang, X. Yang and B. Zhu, *Composites, Part B*, 2020, 108073.
27 C. Wang, X. Li, H. Hu, L. Zhang, Z. Huang, M. Lin, Z. Zhang, Z. Yin, B. Huang and H. Gong, *Nat. Biomed. Eng.*, 2018, **2**, 687–695.
28 Y. Zhang, N. Zheng, Y. Cao, F. Wang, P. Wang, Y. Ma, B. Lu, G. Hou, Z. Fang and Z. Liang, *Sci. Adv.*, 2019, **5**, eaaw1066.
29 Y.-L. Park, C. Majidi, R. Kramer, P. Bérard and R. J. Wood, *J. Micromech. Microeng.*, 2010, **20**, 125029.
30 R. Fu, L. Tu, Y. Zhou, L. Fan, F. Zhang, Z. Wang, J. Xing, D. Chen, C. Deng and G. Tan, *Chem. Mater.*, 2019, **31**, 9850–9860.
31 Q. Shi, T. Wang and C. Lee, *Sci. Rep.*, 2016, **6**, 24946.
32 L. Jiang, Z. Tan, L. Xie, Y. Li, J. Xing, J. Wu, Q. Chen, D. Xiao and J. Zhu, *J. Eur. Ceram. Soc.*, 2018, **38**, 2335–2343.
33 N. H. Gaukås, Q.-S. Huynh, A. A. Pratap, M.-A. Einarsrud, T. Grande, R. D. Holsinger and J. Glaum, *ACS Appl. Bio Mater.*, 2020, **3**, 8714–8721.
34 L. Jiang, R. Chen, J. Xing, G. Lu, R. Li, Y. Jiang, K. Kirk Shung, J. Zhu and Q. Zhou, *J. Appl. Phys.*, 2019, **125**, 214501.
35 C. K. Jeong, J. H. Han, H. Palneedi, H. Park, G.-T. Hwang, B. Joung, S.-G. Kim, H. J. Shin, I.-S. Kang and J. Ryu, *APL Mater.*, 2017, **5**, 074102.
36 Q. Liu, Y. Zhang, J. Gao, Z. Zhou, H. Wang, K. Wang, X. Zhang, L. Li and J.-F. Li, *Energy Environ. Sci.*, 2018, **11**, 3531–3539.
37 Z.-Y. Shen, Y. Xu and J.-F. Li, *J. Appl. Phys.*, 2009, **105**, 104103.
38 Q. Ke, W. H. Liew, H. Tao, J. Wu and K. Yao, *IEEE Trans. Ultrason., Ferroelect., Freq. Control*, 2019, **66**, 1395–1401.
39 Z. Y. Shen, J. F. Li, R. Chen, Q. Zhou and K. K. Shung, *J. Am. Ceram. Soc.*, 2011, **94**, 1346–1349.
40 H. L. W. Chan and J. Unsworth, *IEEE Trans. Ultrason., Ferroelect., Freq. Control*, 1989, **36**, 434–441.
41 Q. Zhou, K. H. Lam, H. Zheng, W. Qiu and K. K. Shung, *Prog. Mater. Sci.*, 2014, **66**, 87–111.

42 H.-W. Wang, N. Chai, P. Wang, S. Hu, W. Dou, D. Umulis, L. V. Wang, M. Sturek, R. Lucht and J.-X. Cheng, *Phys. Rev. Lett.*, 2011, **106**, 238106.
43 A. de la Zerda, J. W. Kim, E. I. Galanzha, S. S. Gambhir and V. P. Zharov, *Contrast Media Mol. Imaging*, 2011, **6**, 346–369.
44 V. V. Yakovlev, H. F. Zhang, G. D. Noojin, M. L. Denton, R. J. Thomas and M. O. Scully, *Proc. Natl. Acad. Sci. U. S. A.*, 2010, **107**, 20335–20339.
45 L. V. Wang and J. Yao, *Nat. Methods*, 2016, **13**, 627.
46 G. Diebold, T. Sun and M. Khan, *Phys. Rev. Lett.*, 1991, **67**, 3384.
47 Z. Yang, D. Zeng, H. Wang, C. Zhao and J. Tan, *Smart Mater. Struct.*, 2015, **24**, 075029.
48 L. Ivey, *NRL-USRD Series F42 Omnidirectional Transducer Standards*, Naval Research Lab, Washington, DC, 1979.
49 T. Li and P. S. Lee, *Actuators*, 2019, **8**, 8–20.
50 K. H. Lee, Y.-Z. Zhang, Q. Jiang, H. Kim, A. A. Alkenawi and H. N. Alshareef, *ACS Nano*, 2020, **14**, 3199–3207.
51 E. J. Lee, T. Y. Kim, S.-W. Kim, S. Jeong, Y. Choi and S. Y. Lee, *Energy Environ. Sci.*, 2018, **11**, 1425–1430.
52 W. Liu, Z. Wang, G. Wang, G. Liu, J. Chen, X. Pu, Y. Xi, X. Wang, H. Guo and C. Hu, *Nat. Commun.*, 2019, **10**, 1–9.
53 Z. L. Wang, J. Chen and L. Lin, *Energy Environ. Sci.*, 2015, **8**, 2250–2282.
54 A. Koka, Z. Zhou and H. A. Sodano, *Energy Environ. Sci.*, 2014, **7**, 288–296.
55 E. Bahat-Treidel, O. Hilt, R. Zhytnytska, A. Wentzel, C. Meliani, J. Wurfl and G. Trankle, *IEEE Electron Device Lett.*, 2012, **33**, 357–359.
56 M. Z. Miskin, A. J. Cortese, K. Dorsey, E. P. Esposito, M. F. Reynolds, Q. Liu, M. Cao, D. A. Muller, P. L. McEuen and I. Cohen, *Nature*, 2020, **584**, 557–561.
57 J. Wu, D. Xiao and J. Zhu, *Chem. Rev.*, 2015, **115**, 2559–2595.
58 A. Colas and J. Curtis, *Biomater. Sci.*, 2004, **2**, 80–85.
59 H. Shankar, P. S. Pagel and D. S. Warner, *J. Am. Soc. Anesthesiol.*, 2011, **115**, 1109–1124.
60 T. A. Bigelow, C. C. Church, K. Sandstrom, J. G. Abbott, M. C. Ziskin, P. D. Edmonds, B. Herman, K. E. Thomenius and T. J. Teo, *J. Ultrasound Med.*, 2011, **30**, 714–734.
61 Prepared by the Safety Group of the British Medical Ultrasound Society, *Ultrasound*, 2010, **18**, 52–59.
62 P. Kamalinejad, C. Mahapatra, Z. Sheng, S. Mirabbasi, V. C. Leung and Y. L. Guan, *IEEE Commun. Mag.*, 2015, **53**, 102–108.
63 T. Meeker, *IEEE Trans. Ultrason., Ferroelectr., Freq. Control*, 1996, **43**, 717–772.

